Planar structured materials with extreme elastic anisotropy

Jagannadh Boddapati, Chiara Daraio

Division of Engineering and Applied Science, California Institute of Technology, Pasadena, CA 91125, USA

A R T I C L E   I N F O

A B S T R A C T

Designing anisotropic structured materials by reducing symmetry results in unique behaviors, such as shearing under uniaxial compression. While rank-deficient materials such as hierarchical laminates have been shown to exhibit extreme elastic anisotropy, there is limited knowledge about the fully anisotropic elasticity tensors achievable with single-scale fabrication techniques. No established upper and lower bounds on anisotropic moduli exist. In this paper, we estimate the range of anisotropic stiffness tensors achieved by single-scale two-dimensional structured materials. We first develop a database of periodic anisotropic single-scale unit cell geometries using linear combinations of periodic cosine functions. The database covers a wide range of anisotropic elasticity tensors, which are then compared with the elasticity tensors of hierarchical laminates. We identify the regions in the property space where hierarchical design is necessary to achieve extremal properties. We demonstrate a method to construct various 2D functionally graded structures using this cosine function representation. These graded structures seamlessly interpolate between unit cells with distinct patterns, allowing for independent control of several functional gradients, such as porosity, anisotropic moduli, and symmetry. When designed with unit cells positioned at extreme parts of the property space, these graded structures exhibit unique mechanical behaviors such as selective strain energy localization, compressive strains under tension, and localized rotations.

1. Introduction

Structured materials are engineered materials that derive special functionality from their micro- and meso- architecture. By fine-tuning the micro- and meso-architecture of both periodic and aperiodic tilings, a diverse range of effective mechanical properties can be achieved beyond what is possible with the corresponding material used for fabrication [1]. As a result, the structured materials help achieve mechanical properties such as negative Poisson ratio [2] that their corresponding base materials could not achieve. Among several mechanical properties of the metamaterials, elasticity tensors provide crucial information related to the energy density stored in the material, and indicate the directions in which the structure is most resistant or compliant to the applied loads. Using structured materials to tune local mechanical properties in the form of elasticity tensors [3,4], it is possible to design mechanical cloaks [5,6], artificial bone scaffolds [7], cardiac stents [8], wearable haptic interfaces [9], and elastic wave manipulating devices [10].

Structured solids are not a new concept. Foams, for example, also derive their properties from their mostly hollow microstructure. However, due to the stochastic nature of the foams' geometries, their elastic properties are isotropic and mostly dependent on the volume fraction of the material [11]. With advances in additive manufacturing, engineers design structured solids beyond foams and architect the material systematically to get desired mechanical behavior by decoupling the strong dependence on the volume fraction. The designs range from simple truss-based lattice materials [12] to intricate spinodoid metamaterials with arbitrary curvatures [13], frequently engineered to exhibit near-isotropic behavior characterized by two elasticity parameters. However, when the elastic properties of structured materials become direction-dependent, more descriptors (elasticity tensor moduli) are required. The mechanical behavior of a completely anisotropic material is described by 6 independent elasticity tensor moduli in two dimensions (2D) and 21 moduli in three dimensions (3D), as opposed to 2 when the properties are direction-independent. Such a high number of independent elastic moduli expands the design space of structured materials. Thus anisotropy allows for coupled deformations, such as materials that can shear under uniaxial compression [14] and shear-shear coupling: where shear deformation in one direction induces shear stresses in a perpendicular direction. These coupled deformations have applications in shape-morphing [15], mode-conversion between longitudinal and shear elastic waves [16], impact mitigation via energy redirection [17] and sound attenuation [18]. Despite many studies on shear-normal coupled

deformations, a comprehensive understanding of their fundamental limits remains inadequate.

Designing metamaterials for anisotropy, despite their ability to attain unique properties, is a challenging task. Besides the fact that fewer or no symmetries in the unit cell design lead to a higher degree of anisotropic properties, the factors that contribute to strong anisotropic behavior with coupled deformations remain largely unexplored. Inverse techniques, such as topology optimization, are frequently used to obtain unit cells that possess desirable elasticity tensor [19,20]. However, such inverse design techniques may not always be the best approach, as it is not known a priori whether the prescribed elasticity tensor is compatible with the provided geometric parametrization. An alternative design approach involves predefined parametrization for the unit cell. This parametrization is then used to compute pre-computed databases, enabling the derivation of useful structure-property relationships [3,4,21–24]. These data-driven methods generate databases that function as quick reference tables, such as for identifying extremal structures at the boundary of the property space, and can serve as initial guesses for topology optimization [25]. They also provide robust datasets for machine learning-based design algorithms [26,27]. For example, using the latent space provided by variational autoencoders (VAEs), Wang et al. [28] demonstrated how to obtain complex topological and mechanical interpolations in various unit cells. Similarly, Mao et al. [29] used generative adversarial networks (GANs) to discover new stiffer unit cells beyond the training data. By leveraging the gradients provided by artificial neural network models, it is now possible to perform inverse designs customized to specific anisotropic elasticity tensors [30–32] and further to tailor nonlinear mechanical behavior [33–35]. While these unique approaches can identify unit cells with diverse elasticity tensors beyond the isotropic class, the range of achievable properties is primarily constrained by the selected input design representation. Additionally, most of these approaches are restricted to orthotropic elasticity, where coupled deformations are absent. There is limited knowledge about the range of elasticity tensors, especially concerning the extent to which shear-normal deformations can be coupled in two-dimensional single-scale structured materials.

On one hand, achieving a complete characterization of the parameter space in terms of the moduli becomes exceedingly difficult in the absence of a unique parametrization of the input geometry. On the other hand, defining how close the obtained designs are to the theoretical bounds is also challenging, as little is known about the theoretical limits of anisotropic elastic moduli (no known closed-form expressions) [36]. This range of all possible effective tensors is mathematically known as *G-closure*. In classical studies on isotropic composites, Hashin and Shtrikman [37,38] present a variational approach to determine the upper and lower bounds on the effective bulk and shear moduli (κ^* and μ^*) by decomposing the elastic energy into hydrostatic and deviatoric parts. Hence, the bulk and shear moduli directly represent the energy that can be stored in the composites under hydrostatic and deviatoric loading respectively. However, individual parameters in the fully anisotropic case do not hold such straightforward interpretations. Even in the isotropic case, there are areas in the property space of μ^* defined by theoretical bounds where composites are yet to be discovered [36]. Willis [39], Milton and Kohn [40], Cherkaev and Gibiansky [41], Allaire and Kohn [42] extended the theory of Hashin-Shtrikman isotropic bounds to orthotropic elasticity tensors, by introducing "trace-bounds". These trace bounds, categorized as 'bulk modulus type' and 'shear moduli type', are derived by bounding the trace of the inverse stiffness tensor (compliance tensor) projected onto specific tensor subspaces. These calculations only establish bounds on a certain combination of elastic moduli. Moreover, extending this method to fully anisotropic media with shear-normal coupling is non-trivial. This is because the energy cannot be decomposed into simple tensor components but involves a combination of them for any type of loading.

To bridge this gap, Milton and Camar-Eddine [43] expanded upon the theories proposed by Willis [39], Allaire and Kohn [42] on isotropic

composites to explore bounds on arbitrary stress-strain pairs in the anisotropic composites. The key finding from this work is that sequentially layered laminates are shown to achieve these bounds on stress-strain pairs. By examining the sum of energy and complementary energies, they show that integrating a rank-deficient material, such as a pentamode metamaterial within hierarchical laminates enables the attainment of extremality in the stress-strain space. Pentamode materials were first introduced by Milton and Cherkaev [44], suggesting that using pentamode materials as fundamental building blocks allows for the achievement of arbitrary effective anisotropic properties [45]. Generally, elasticity tensors of extremal materials exhibit rank deficiency [46,47], a characteristic shared by pentamode materials and hierarchical laminates. Additionally, hierarchical laminates also emerge as energy-minimizing optimal structures in various microstructure evolution problems [48–51], as they are shown to achieve constant stress or strain in one of the phases and leading to the optimization of the translation bounds [52].

While hierarchical structures and other rank-deficient materials could serve as a design guide in realizing extreme elastic anisotropy, physically realizing such structures demands advanced fabrication techniques that are still in development. There is limited knowledge about the elasticity tensors achievable with single-scale fabrication techniques. In this paper, we address this gap by sampling a diverse database of anisotropic unit cells created by combining periodic cosine functions of varied spatial frequencies, as discussed in Section 2. The database properties are then compared with the properties of hierarchical laminates in Section 3 for the first time (to the best of our knowledge) which are considered as theoretical bounds. This comparison helps identify the regions in the property space where hierarchical designs necessary to achieve extreme elastic anisotropy. In Section 4, we demonstrate a method to construct various functionally graded structures using this cosine function representation for the unit cells. We show that the graded structures seamlessly interpolate between unit cells with distinct patterns. We then analyze the mechanical behavior of two such graded structures to achieve energy localization and strain localization, utilizing unit cells with extreme anisotropy in the graded design. Finally, we provide concluding remarks in Section 5.

2. Generating a diverse unit cell database

Our goal is to identify the range of effective anisotropic elasticity tensors that can be achieved from periodic single-scale unit-cells composed of two isotropic phases. To accomplish this, we use a pixelated representation for the unit cell geometry parametrization. Exploring all possible combinations of two phases in this pixelated representation is computationally NP-hard.[1] Therefore, to sample periodic diverse anisotropic unit cells efficiently with lower degrees of symmetry, we follow an approach introduced in our prior work [53]. This approach is inspired by Cahn's method of generating Gaussian random fields [13,30,54]. Additionally, this method is inspired by the observation that the power spectral density of microstructures in metallic systems tends to be sparse and has peaks highly concentrated at lower spatial frequencies [55,56], explained in detail in Appendix A.1 and Fig. A.10. We first define a periodic function $f(x_1, x_2)$, as a linear combination of cosine functions:

$$f(x_1, x_2) = \sum_{m,n} A_{mn} \cos\left(2\pi(mx_1 + nx_2)\right),$$

$$\forall (x_1, x_2) \in [-0.5, 0.5], \quad \forall m, n \in \mathbb{Z}, \tag{1}$$

where m, n are spatial frequencies, and A_{mn} are the corresponding cosine function weights Fig. 1A. The function is then thresholded at different values, to generate a family of unit cells, as shown in Fig. 1B.

---

[1] For example, a 100 × 100 periodic pixelated representation requires the computation of mechanical properties of $2^{99 \times 99} = 2^{9801}$ unit cells.
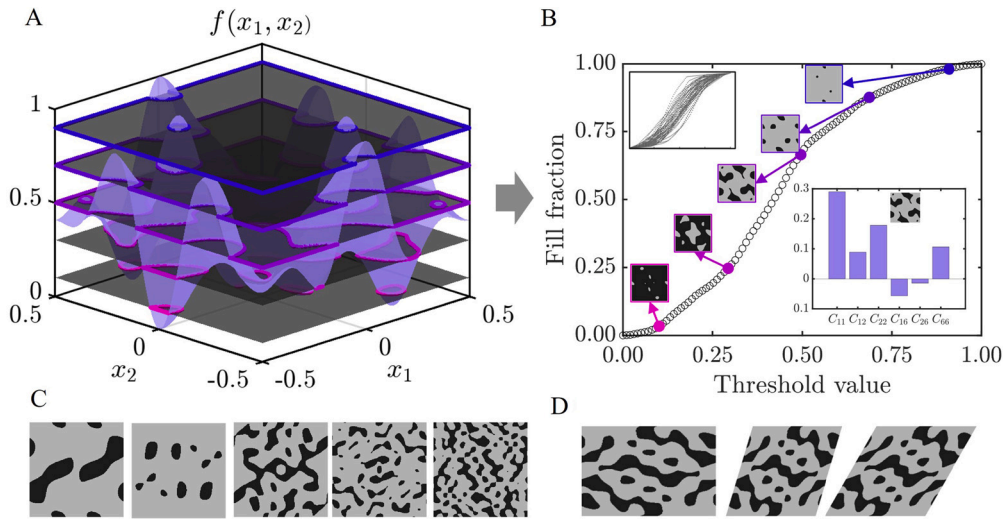
Fig. 1. (A) Various anisotropic unit cells can be sampled by thresholding periodic functions composed of several cosine spatial modes, (B) Variation of unit cell patterns with the fill fraction of the stiff phase as the threshold value is changed from 0 to 1 for a particular periodic function. The elastic properties of a unit cell normalized with Young's modulus of the stiff phase (bottom-inset), and the variation of the threshold–fill fraction curve for different realizations of the periodic function (top-inset). (C) As the number of spatial modes is increased, finer patterns arise in the designs and unit cells tend to be less anisotropic, (D) To generate non-square unit cells, the directions along which the function is periodic can be varied. Rectangular, oblique, and rhombus-shaped unit cells are shown for a fixed unit cell pattern.

Several notable observations can be made for this approach. Firstly, the periodicity in the unit cells is ensured by directly selecting cosine functions. Interestingly, choosing between sine and cosine as the fundamental periodic function does not affect the distribution of the resulting properties. We pick the weights as independent random variables uniformly distributed between -1 and 1. However, there are no constraints on the range of the coefficients A_{mn} as the function is always normalized to fall in the range from to 1 before thresholding. By controlling the symmetries in the weights, we can control the symmetries in the unit cell. For instance, if $A_{mn} = A_{nm}$, the result is diagonally symmetric unit cells. A detailed discussion on the choice of A_{mn} and its effect on the symmetries of the geometry and the elasticity tensor is included in the Appendix A.1. Adjusting the pixel density allows us to generate unit cells with arbitrary resolutions as need-based. By increasing the threshold value of the function Eq. (1), the fill fraction of the stiff phase increases monotonically. Each function exhibits a different rate of monotonic increase in the fill fraction, as illustrated in the top inset of Fig. 1B. In this particular work, a few refinements have been made to our previous design approach [53]. The number of spatial modes is a hyperparameter $2\zeta+1$, with $\zeta = \max(m,n)$. In Fig. 1C, the variation of typical feature sizes is shown when the number of spatial modes is varied. Increasing the number of spatial modes leads to smaller feature sizes and increased randomness, resulting in unit cells that tend to be less anisotropic. The shape of the unit cell is also an important factor for achieving anisotropic properties and is a design choice that is often overlooked. By modifying the directions of periodicity in the proposed periodic function definition Eq. (1), we can also generate non-square unit cells as shown in Fig. 1D (explained in detail in Appendix A.2). Overall, this method allows us to systematically explore a large property space, identify structures that exhibit the desired anisotropic elasticity tensors and is suitable for estimating theoretical bounds on the anisotropic moduli, as discussed in the next section. Further, the coefficients A_{mn} are sampled randomly to generate 2000 different functions and the threshold is varied for 100 increments resulting in a database size of 200000 unit cells as opposed to only 100 unit cells in our previous work [53].

Each unit cell's effective material properties are then computed using a numerical homogenization scheme [57,58]. The homogenization scheme is based on length scale separation and follows a two-scale asymptotic expansion of stress equilibrium equation. The resulting effective properties are equivalent in the average energy stored in the

unit cell for all possible loading conditions. In computing the effective properties, we fix the pixel resolution at 100. For the gray phase, we use a stiffer material DM8530 ($E = 1$ GPa, $v = 0.3$) and for black phase, we use a softer material Tango Black ($E = 0.7$ MPa, $v = 0.49$), representative of materials from commercial multi-material Connex 3D printer. The material properties are experimentally determined following the ASTM D638-14 standard test method. We follow Voigt notation to describe the homogenized constitutive law, assuming plane-strain condition as

$$\begin{bmatrix} \sigma_1 \\ \sigma_2 \\ \sigma_6 \end{bmatrix} = \begin{bmatrix} C_{11} & C_{12} & C_{16} \\ C_{12} & C_{22} & C_{26} \\ C_{16} & C_{26} & C_{66} \end{bmatrix} \begin{bmatrix} \varepsilon_1 \\ \varepsilon_2 \\ 2\varepsilon_6 \end{bmatrix}. \tag{2}$$

where $C_{11}, C_{12}, C_{22}, C_{16}, C_{26}, C_{66}$ are the six independent elasticity tensor parameters in a given reference frame, $\varepsilon_1, \varepsilon_2$ are the axial strains, ε_6 is the shear strain, σ_1, σ_2 are the axial stresses, and σ_6 is the shear stress. The homogenized elastic properties of one of the unit cells, normalized with Young's modulus of the stiff phase, are shown in Fig. 1B (bottom inset). In order to satisfy thermodynamic stability, parameters along the diagonal of Eq. (2) are always positive, while the parameters on the off-diagonal could be negative. C_{11} directly relates the axial stress σ_1 with axial strain ε_1, while C_{16} relates the axial stress σ_1 with shear strain σ_6, and so on. The off-diagonal moduli C_{16}, C_{26} are also known as shear-normal coupling parameters. We aim to determine the maximum and minimum values a single parameter can reach relative to the others, as discussed in the following section. This understanding helps us evaluate the extent of shear-normal coupling induced by anisotropy.

3. Data visualizations

3.1. Fill fraction plots

In Fig. 2, the data of material properties C_{11}, C_{12}, C_{16} is plotted as a function of the fill fraction of the stiff phase. Analogous plots of the effective homogenized bulk modulus (κ), shear modulus (μ) and Poisson's ratio (v) are shown in Fig. S1. All the parameters are normalized with Young's Modulus of the stiff phase. Note that C_{22}, C_{66} have similar property distribution as that of C_{11} while C_{26} property distribution is similar to C_{16} and hence these parameters are not plotted for brevity. As there are no closed-form expressions for the theoretical bounds on anisotropic
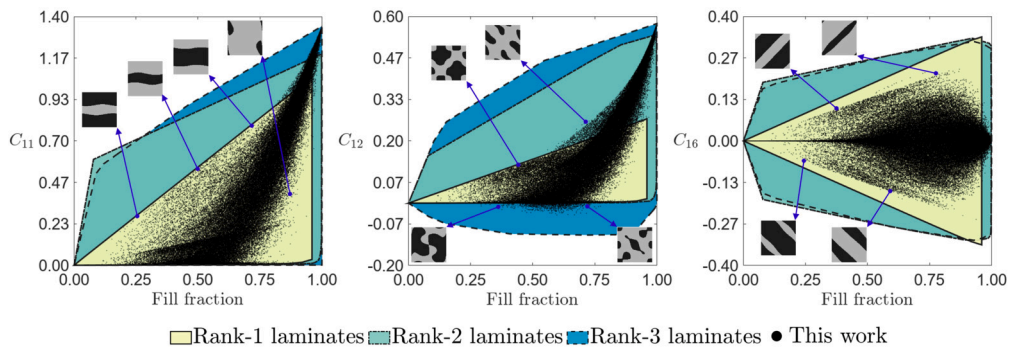
Fig. 2. Plots of fill fraction of stiff phase vs. (A) C_{11}, (B) C_{12}, (C) C_{16} from this database. All the plots are normalized with the Young's modulus of the stiff phase. Properties of hierarchical laminates are used as theoretical bounds. Rank-1 laminates are indicated with lime yellow color, rank-2 laminates are indicated with green color and rank-3 laminates are indicated with blue color. Representative unit cells at the boundary are pointed out using arrows. The unit cells away from the bounds contain non-trivial patterns and some of them are displayed in the subsequent figures. In the plot of the fill fraction vs. C_{16}, both rank-2 and rank-3 laminates achieve nearly the same range.

moduli, the range of properties achieved by hierarchical laminates upto rank-3 is used as a substitute and indicated in the same plots. Please refer to Appendix A.3 for a discussion on theoretical bounds and Appendix A.4 and Fig. A.11 for the construction and computation of the effective properties of the hierarchical laminates. First, we observe that in all property plots, rank-2 laminates (shown in green) significantly expand the property range compared to rank-1 laminates (shown in lime yellow). However, the transition from rank-2 to rank-3 laminates (shown in blue) shows minimal improvement across all moduli except for C_{12}. For C_{12}, the negative region is only accessible with rank-3 laminates, and this range shows minimal dependence on the fill fraction beyond 25%. Both rank-2 and rank-3 laminates reduce the strong dependence on achieving higher values for specific moduli, allowing stiffer anisotropic properties beyond linear scaling with a low fraction of the stiff phase. Additionally, hierarchical laminates demonstrate that using anisotropic constituent phases can significantly enhance the range of achievable properties in single-scale two-phase composites.

Our database consisted of unit cells achieving the bounds predicted by rank-1 laminates, specifically in the fill fraction ranging between 30% - 80%. To understand the effect of spatial frequencies, the same plots are plotted in different colors with data constructed from adding a specific number of spatial frequencies (Fig. S2). It is observed that adding higher spatial modes doesn't necessarily increase the reach in the property space. In fact, adding higher spatial modes is detrimental to producing anisotropic structures beyond spatial modes of order 3. While square unit cells were sufficient to explore the extremes of the diagonal moduli, the range of the off-diagonal moduli is enhanced with the use of non-square unit cells (Fig. S3). For C_{11}, the structures at the upper bound are laminate-like structures aligned along the x_1 direction, while those at the lower bound are laminates aligned along the x_2. For C_{12}, the unit cells at the upper and lower bounds are non-laminate-like. In the negative C_{12}, the discovered unit cells do not approach the bounds of rank-3 laminates and feature chiral patterns and/or orthogonally aligned thin features. For C_{16}, the upper bound unit cells are skew laminates tilted towards right, while those at the lower (negative) bound are the same skew laminates, but flipped.

Hierarchical architectures play a significant role in structural integrity and functionality across systems of various length scales (e.g. spider silk) [59]. This hierarchy is often present in non-rectangular coordinate systems. For example, wire ropes used in structural engineering contain helical strands arranged in a hierarchical manner, enhancing efficient load transfer and their strength by distributing tensile forces uniformly throughout the cross-section, regardless of the bending direction [60]. In biological systems, spinal discs, which are annular cylinders surrounding the spine in the vertebrae, provide shock absorption, support, and flexibility to the spine. Their load-bearing protein, collagen, is distributed in a multi-layered laminar fashion [61]. Similarly, the tym-

panic membrane of the human ear, which is responsible for efficient sound transmission and protecting the delicate structures within the ear, is conical in shape and features collagen structured in a trilaminar fashion with radial and circumferential patterns [62]. These observations along with findings from our work further emphasize the importance of incorporating hierarchical designs to enhance the design capabilities.

3.2. Pair property plots

Often, multiple components of the elasticity tensor contribute to the overall mechanical behavior. Therefore, we also examine the pair property plots. For a total of 6 material parameters, there are a total of $\binom{6}{2} = 15$ distinct pair property plots. However, due to the symmetry nature of the property plots, it is sufficient to consider only a subset of the plots. For example, the property plot of C_{11} vs C_{16} would be the same as C_{22} vs C_{26}. As the goal of this paper is to identify anisotropic structure-property relations, specifically shear-normal coupling, the property plots associated with the off-diagonal parameters of the elasticity tensor are discussed in detail. Therefore, the property plots corresponding to C_{16} vs. C_{26}, C_{16} vs. C_{12}, C_{11} vs. C_{22}, C_{66}. C_{12} are shown in Fig. 3. Please refer to Fig. S4 for the rest of the pair-property plots. In the same plots, as discussed earlier, the range of properties achieved by hierarchical laminates is used as a substitute for theoretical bounds. Each laminate class data is plotted separately in Figs. S5 to S7 to highlight their differences.

In the property plot of C_{16} vs. C_{26} shown in Fig. 3A, we observe that there is a strong correlation along the line inclined at 45°. This means for many of the unit cells, both C_{16} and C_{26} have the same sign. Hierarchical laminates uncorrelated this behavior and achieved unit cells with opposing signs for C_{16} and C_{26}. The unit cells identified on the boundary of this property space resemble rank-1 laminates. As discussed in [63], $C_{16} + C_{26}$ and $C_{16} - C_{26}$ are components of the invariants of the elasticity tensor under coordinate transformation. Each of these sums signifies a different contribution to the stored elastic energy (see Eqs. (S11) and (S12) in Appendix S-I). In the property plots of C_{66} vs. C_{12} and C_{11} vs. C_{12} shown in Fig. 3E-F, there are generally very few data points with a negative value of C_{12}, especially at high values of C_{66}. Again, the negative region for C_{12} is only accessible with rank-3 laminates. The combination $\kappa = \frac{1}{4}\left(C_{11} + C_{22} + 2C_{12}\right)$, known as the bulk modulus, is an invariant. This imposes a restriction on the negative bound of C_{12} to ensure that κ remains positive. The parameter $C_{66} - C_{12}$ is invariant under coordinate transformation. Therefore, C_{66} vs. C_{12} plot for rank-1 laminates is strictly a single linear line. C_{66} vs. C_{12} plot for rank-2 and rank-3 laminates is composed of several such lines with different slopes, which is clearly observed in Fig. S6. Note that the elasticity tensor bounds are also dependent on the Poisson's ratio of the softer phase [64] especially if the soft phase is near incompressible. However, we did not study the effect of this parameter on the bounds in this paper.
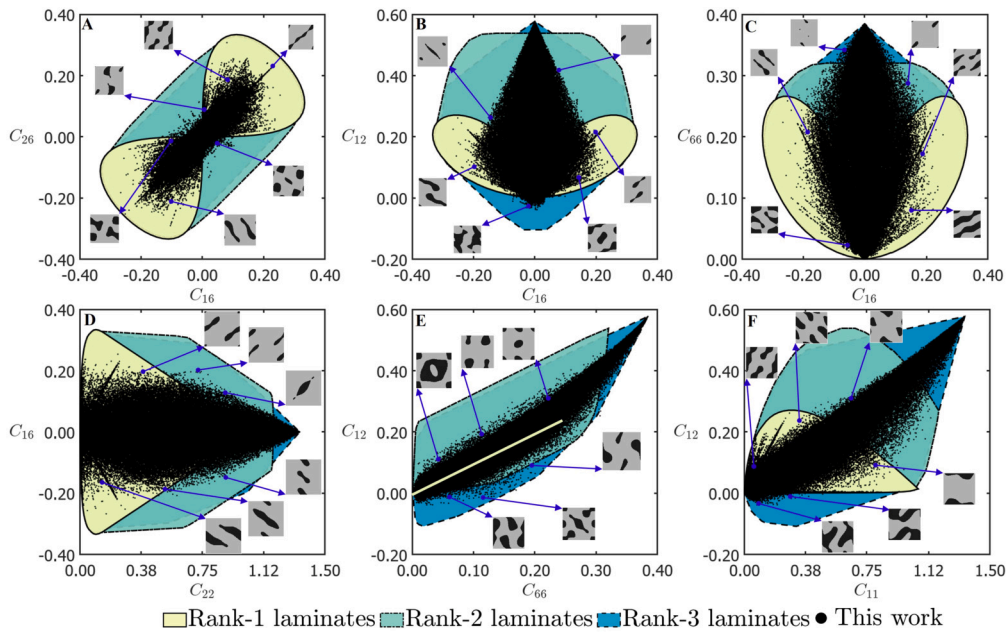
Fig. 3. Plots of (A) C_{16} vs. C_{26}, (B) C_{16} vs. C_{12}, (C) C_{16} vs. C_{66}, (D) C_{22} vs. C_{16} (E) C_{66} vs. C_{12} and (F) C_{11} vs. C_{12} from this database. All the plots are normalized with the Young's modulus of the stiff phase shown in gray color. Rank-1 laminates are indicated with lime yellow color, rank-2 laminates are indicated with green color and rank-3 laminates are indicated with blue color. Representative unit cells at the boundary are pointed out using arrows. In the plot of C_{16} vs. C_{26}, both rank-2 and rank-3 laminates achieve nearly the same range.

To validate the effective homogenized behavior of unit cells, we conducted experiments on finite tessellations of four different unit cells in a separate study [53]. In this study, we successfully identified all the anisotropic moduli including shear-normal coupling parameters. The results showed that at least 10 repeated unit cells in the tessellated structure are required to satisfy homogenization conditions.

4. Functionally graded structures

4.1. Method of generation of functionally graded structures

Functionally graded structures have been shown to exhibit unique mechanical behavior such as enhanced energy absorption [65], avoiding shear-banding [66] and, mimicking bone stiffness [30]. To generate such structures, often the parametrization associated with the structure such as truss thickness is adjusted [67–69]. Therefore, these approaches are particularly effective in controlling the isotropic Young's Modulus, relative density, and to some extent, the degree of orthotropic elasticity [70,71]. However, achieving smooth spatial gradients in the anisotropic mechanical properties while ensuring the connectivity of adjacent unit cells is challenging. Here, we illustrate the construction of functionally graded anisotropic structures with seamless transition between unit cells with distinct patterns.

For this purpose, we use the proposed functional representation used to generate unit cells in Section 2. We introduce the local variables x_1, x_2 as well as the global variables X_1, X_2. The global variables are defined only on a coarser grid, while the local variables are defined on a finer grid. In a graded structure with $p \times q$ unit cells, with $p, q \in \mathbb{Z}^+$, the global variables change at discrete locations given by the unit cell centers, while the local variables X_1, X_2 change at each pixel location within the unit cell at a given x_1, x_2. The function that is required to generate the graded structure $h(x_1, x_2, X_1, X_2)$ is thus given by

$$h(x_1, x_2, X_1, X_2) = \beta(X_1, X_2)f_1(x_1, x_2) + \alpha(X_1, X_2)f_2(x_1, x_2), \quad (3a)$$

$$= \beta(X_1, X_2) \sum_{m,n} A_{mn} \cos\left(2\pi(mx_1 + nx_2)\right)$$

$$+ \alpha(X_1, X_2) \sum_{m,n} B_{mn} \cos\left(2\pi(mx_1 + nx_2)\right), \quad (3b)$$

where $\alpha(X_1, X_2)$, $\beta(X_1, X_2) \in [0, 1]$ are weighing parameters such that $\alpha(X_1, X_2) + \beta(X_1, X_2) = 1$. An increase in α signifies the increase in the contribution of second function $f_2(x_1, x_2)$ in the interpolated unit cell. The threshold to generate graded structure from the function is subsequently set by a bilinear interpolation determined by the thresholds set for the unit cells at the ends. This method allows for independent control of several functional gradients, such as porosity, anisotropic moduli, and symmetry. In Fig. 4A-D, various functionally graded structures are shown with different gradients along the X_1-axis using Eq. (3a) while maintaining periodicity along the X_2-axis. Fig. 4E-F shows the bilinear interpolation between four unit cells with different anisotropic behavior at four corners of the boundary. By using nonlinearly interpolated weighing parameters, various graded designs such as radial, elliptical, spiral, star, and many more can be created. Fig. 5 illustrates the designs interpolated non-linearly using the unit cells depicted in Fig. 4C. More examples on the graded designs are added to the supplementary information (see Fig. S8, Fig. S9, Fig. S10, Fig. S11, Fig. S12). In the next section, we investigate the mechanical behavior in two gradient structures with nonlinear interpolations in eliciting atypical mechanical behavior.

4.2. Mechanical behavior of graded structures

4.2.1. Selective elastic energy localization

Energy localization refers to the phenomenon where strain energy in a material or structure is concentrated in specific regions. Energy localization finds use in applications such as mechanical sensing [72], and energy harvesting [73]. Here we show that graded structures with anisotropic unit cells achieve selective energy localization, i.e., different localization behavior under different loading conditions. We achieve this using functionally graded structures with strategically selected unit cells in a radially interpolated design. The unit cells are chosen such that unit cell #1 at the boundary is obtained by a 90° rotation of the unit cell #2 at the interior. The fill fraction of the stiff phase of both the unit cells is 80% respectively. Therefore, this choice makes most of the unit cells in the 20 × 20 interpolated structure also have uniform fill fractions close to 80%. A uniform fill fraction is selected in the graded design to isolate the impact of differences in stiffness parameters from
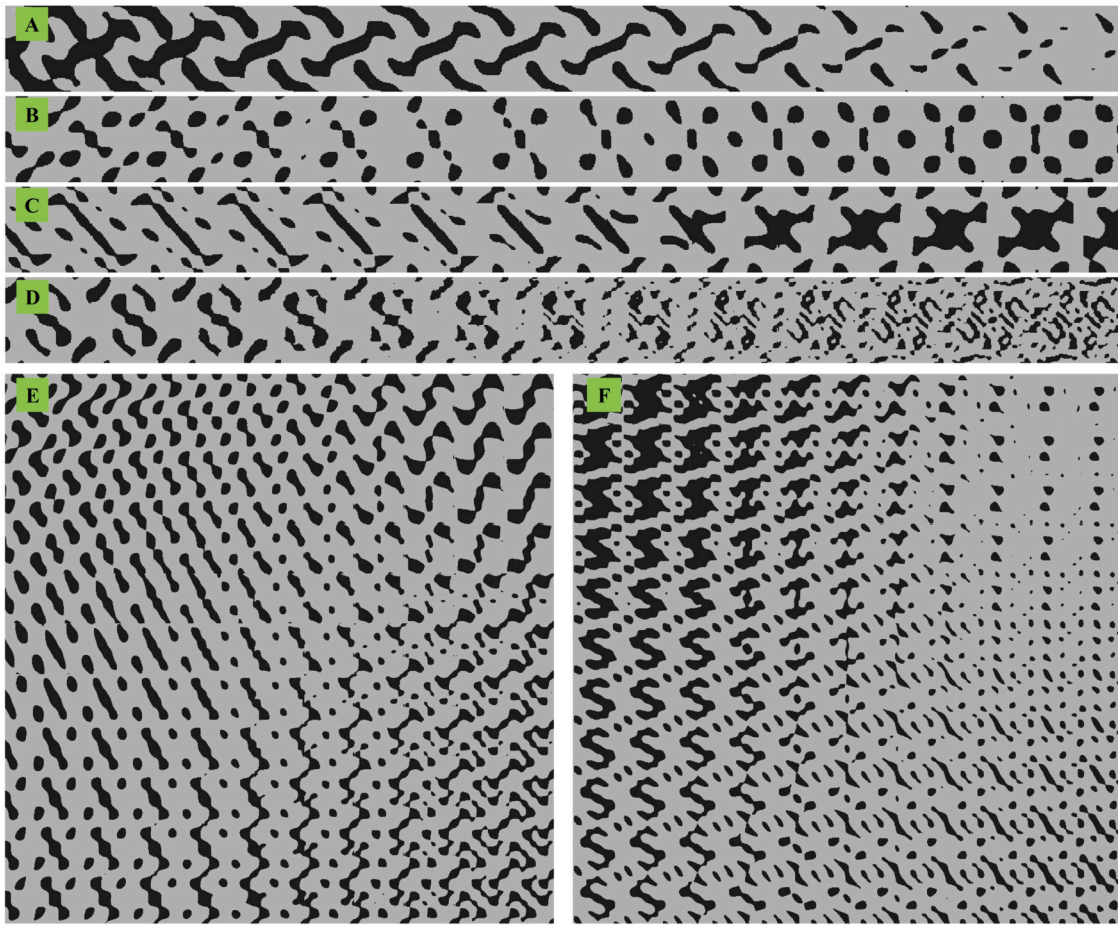
Fig. 4. Functionally graded anisotropic metamaterial generation between two unit-cells with different spatial characteristics such as (A) increasing fill fraction of the stiff phase while using the same periodic function, (B) interpolation from asymmetric to symmetric unit-cells by changing the symmetry in the function weights, (C) interpolation between two asymmetric structures with distinct anisotropic properties, (D) interpolation between unit-cells with an increasing number of spatial modes in the periodic function, (E, F) bilinear interpolation between four unit cells with different anisotropic behavior at four corners of the boundary.

unit cells that may also be affected by varying fill fractions. The (vectorized) stiffness tensor of the unit cell #1 at the boundary is [0.698 0.131 0.221 0.138 0.095 0.150]^T.[2] Therefore, the (vectorized) stiffness tensor of the unit cell #2 is [0.221 0.131 0.698 0.095 0.138 0.150]^T.

We subject this graded structure to three different loading conditions namely, tension along x_2 direction, simple shear along applied on the top edge towards x_1 direction, and a biaxial tensile loading by prescribing a displacement of 1.5 mm. In Fig. 6, the elastic energy density stored in the structure, defined as $W = \frac{1}{2}\sigma : \varepsilon$ is obtained from finite element analysis (FEA). Here we have used the Einstein summation convention, assuming summation over repeated indices, and the double dot ":" indicates a double contraction of indices. The energy density is plotted first just in the stiff phase, then as areal (volumetric) average at each unit cell while including both the phases. The energy distribution is then compared with an effective isotropic medium. The isotropic equivalent is calculated by replacing unit cell with a material whose bulk and shear moduli are that of Hashin-Shtrikman upper bound for the corresponding fill fraction. We observe that under tensile loading the energy distribution becomes significantly localized in a few unit cells in the central region. In contrast, for the simple-shear boundary condition, the energy is localized in the diagonal region. For the biaxial loading con-

dition, energy is distributed in the region exterior to the center.[3] The unit cell #2 in the interior has a higher C_{22} compared to the unit cell #1 at the boundary. Therefore, under tensile loading along x_2 direction, the interior region acts stiffer compared to the exterior region. This geometric frustration results in increased stresses in the interior region. Subsequently, the energy is significantly localized in the center. As for shear loading, the shear-normal coupling in the unit cells distributes the stresses along the identified diagonal region. In the biaxial loading condition, although the fill fraction of all the unit cells is almost same, the interior region is under relatively lower stresses. If both the unit cells were to be isotropic, this distinctive energy localization is not seen. The gradient structures can thus localize energy which can be programmed to have a specific failure mode and/or localize stresses and strains in a preprogrammed location. We further demonstrate the general applicability of this effect when tested with two other unit cells (see Fig. S13).

While plotting the energy density distribution provides valuable insights, localization occurs due to all stress and strain components. To delve deeper into this, we select unit cells where the interior region contains those with negative values for C_{12}, while the exterior region contains positive values for C_{12}, as depicted in Fig. 7. The (vectorized) stiffness tensor of the unit cell #1 (UC1) at the boundary is [0.134 0.082 0.370 -0.050 -0.120 0.107]^T. Similarly, the (vectorized) stiffness ten-

---

[2] In the vectorized format, the stiffness components are ordered as $[C_{11}, C_{12}, C_{22}, C_{16}, C_{26}, C_{66}]^T$.

[3] It should be noted that the maximum value of the energy density for three loading cases is different. We are interested in the distribution over the exact values of the energy density.
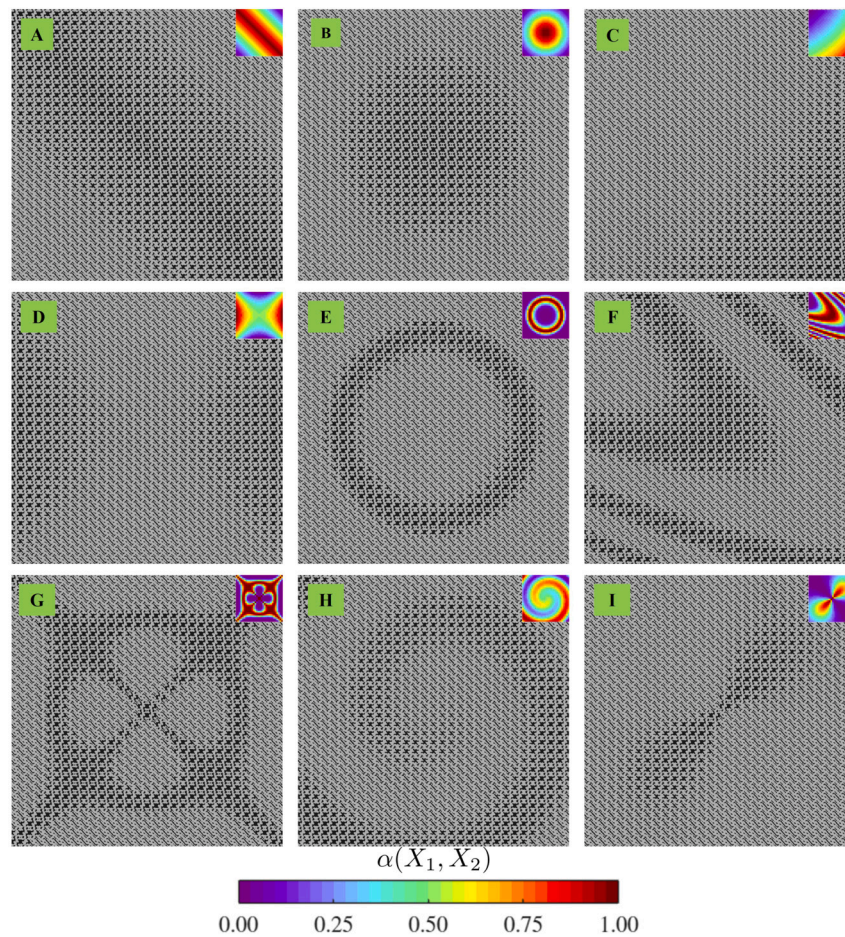
Fig. 5. Functionally graded metamaterials with various nonlinear interpolations: (A) diagonal, (B) circular, (C) semi-circular, (D) hyperbolic, (E) annular, (F) parabolic, (G) star, (H) spiral, and (I) orbital. The inset colormap illustrates the variation of the interpolation parameter $\alpha(X_1, X_2)$, transitioning from blue to red, showing how it changes from one unit cell to another. Each graded structure contains 30×30 unit cells. The 1D linear gradient depicted in Fig. 4C is utilized for all the nonlinear interpolations presented.

sor of the unit cell #2 (UC2) in the interior is [0.171 -0.009 0.096 0.001 -0.017 0.248]^T. The fill fraction of the stiff phase for the unit cells is [73.7%, 59.2%] respectively. The behavior of this design under tensile loading is studied. In this specific scenario, we observe that unit cells in the interior exhibit chiral characteristics, resulting in lateral expansion akin to auxetic behavior. Conversely, unit cells in the exterior, lacking chirality, contract laterally under tensile loading. This geometric mismatch compels interior unit cells to experience compression despite their inherent tendency to expand. Consequently, the region with softer-like properties bears greater stresses and strains, leading to a concentration of energy in the center.

4.2.2. Non-affine deformations

Non-affine deformations refer to deformations of a material where the local strain or displacement of the material points does not follow the global deformation applied to the material. Often soft materials such as polymers, biological tissues, and granular systems exhibit non-affine deformations due to the rearrangement of molecules, particles and/or grains [74,75]. Such non-affine deformations play a crucial role in energy dissipation.

Here, we present an example of inducing non-affine deformations in metamaterials on a global scale by utilizing functionally graded structures with strategically selected unit cells. The two unit cells selected for interpolation are chosen such that their off-diagonal shear-normal coupling moduli are opposite in sign while the other moduli and fill fraction are comparably close. We then create an annular interpolated structure as discussed in Fig. 5C with 20 unit cells along each axis. Please refer to

Fig. S14 for more details on the selection of unit cells and their interpolation. The (vectorized) stiffness tensor of the unit cell in the boundary upon normalization is [0.374, 0.101, 0.108, 0.134, 0.066, 0.110]^T. The (vectorized) stiffness tensor of the unit cell in the annular region upon normalization is [0.115, 0.121, 0.494, -0.084, -0.147, 0.138]^T. The fill fraction of the stiff phase for the unit cells is [62.7%, 69.5%] respectively. As a result, most of the unit cells in the 20 x 20 interpolated structure have fill fractions close to 65%.

This structure is subjected to a tensile loading along x_2 direction by prescribing a displacement of 1.5 mm at the top end. In Fig. 8, the numerical simulations (assuming linear elasticity) reveal that the horizontal displacements exhibit a rotation-like characteristic under this tensile loading. We further experimentally corroborate the same behavior using full-field measurements obtained using digital image correlation (DIC) [76–78]. More details on the experimental procedure can be found in Appendix S-II. The difference in the vertical component of the displacement field (U_2) is minimal. The horizontal component of the displacement field (U_1) from experiments aligns well with the simulation in the annular region (around the central region of the specimen). However, the difference in the horizontal component is significant at the top-right and bottom-left boundaries. A plausible explanation for such deviation could be local material nonlinearity due to stress concentrations. Although our simulations assumed planar deformations, these additively manufactured specimens actually undergo complex three-dimensional deformations [79]. This is discussed in detail further in Fig. S17.

This non-affine deformation behavior seems to arise from the incompatibilities in the off-diagonal shear-normal coupling moduli (C_{16}, C_{26})
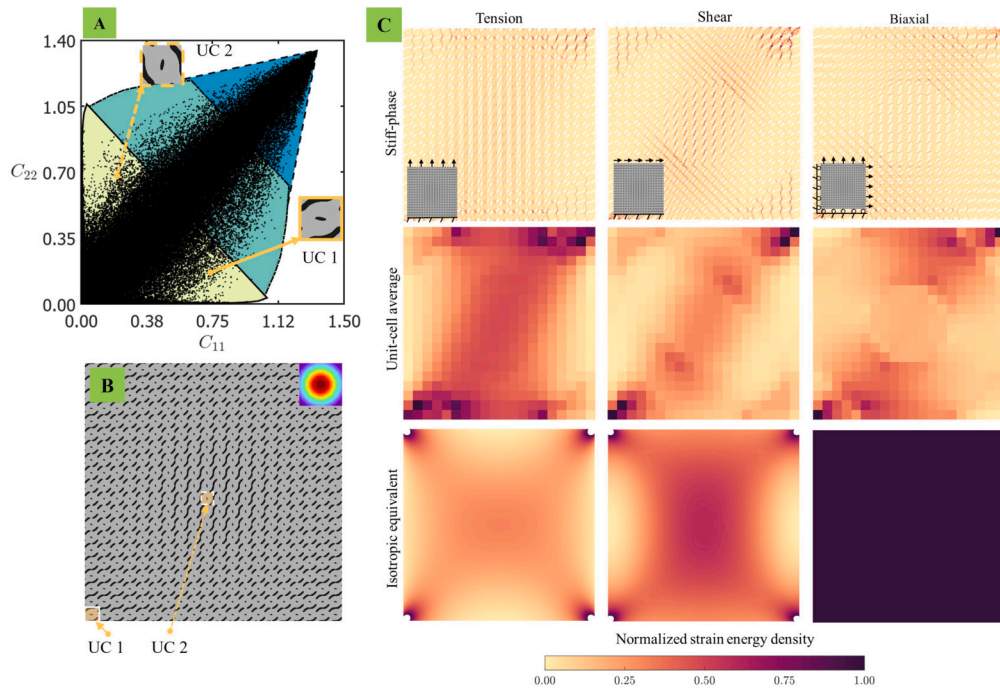
Fig. 6. Demonstration of selective energy localization: (A) Unit cell selection based on the extremity in the property space plot of C_{11} vs. C_{22}. (B) Radially graded design with 20×20 tessellation from the chosen unit cells named UC1, UC2. The inset color map shows the variation of interpolation parameter $\alpha(X_1, X_2)$. (C) Distribution of (normalized) elastic energy stored in the circularly interpolated structure for tensile, shear, and biaxial loading displaying selective energy localization arising from anisotropy of the unit cells. The first row shows the energy distribution in just the stiff phase, the second row shows the energy averaged over each unit cell, the third row shows the energy distribution in a continuum-isotropic equivalent.
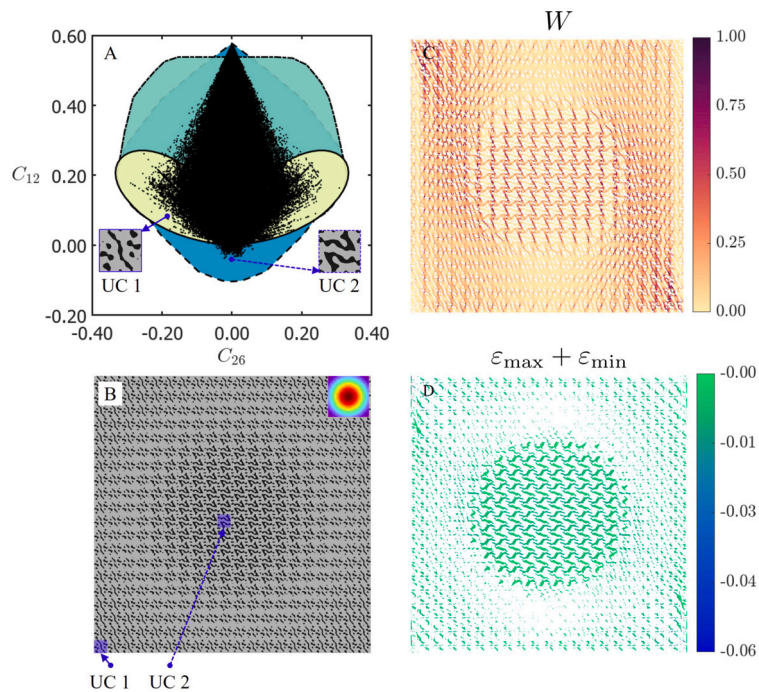

Fig. 7. Compressive strains under tensile loading: (A) Unit cell selection based on the extremity in the property space plot of C_{26} vs. C_{12}, such that (B) the radially graded design from the selected unit cells that can be additively manufactured using only the stiff phase. (C) Normalized energy distribution in the stiff phase under tensile loading applied along x_2 direction. (D) The plot of the sum of principal strains (compressive part only) in the stiff phase which shows compressive strains in the interior region of the radially graded design under the applied tensile loading. Due to geometric incompatibility, the unit cells in the interior undergo compressive strains and compressive stresses under tensile loading.

between the two selected unit cells. The unit cells with positive shear-normal coupling moduli have a preferential direction to shear under tension, which is opposite to the preferential direction of the unit cells with negative shear-normal coupling moduli. Therefore this incompati-

bility in the preferential direction to shear under tension creates internal torque and directs the annular region to rotate while extending in the x_2 direction. In Fig. S15, we demonstrate that the observed behavior can also be seen in other pairs of unit cells with opposing shear-normal
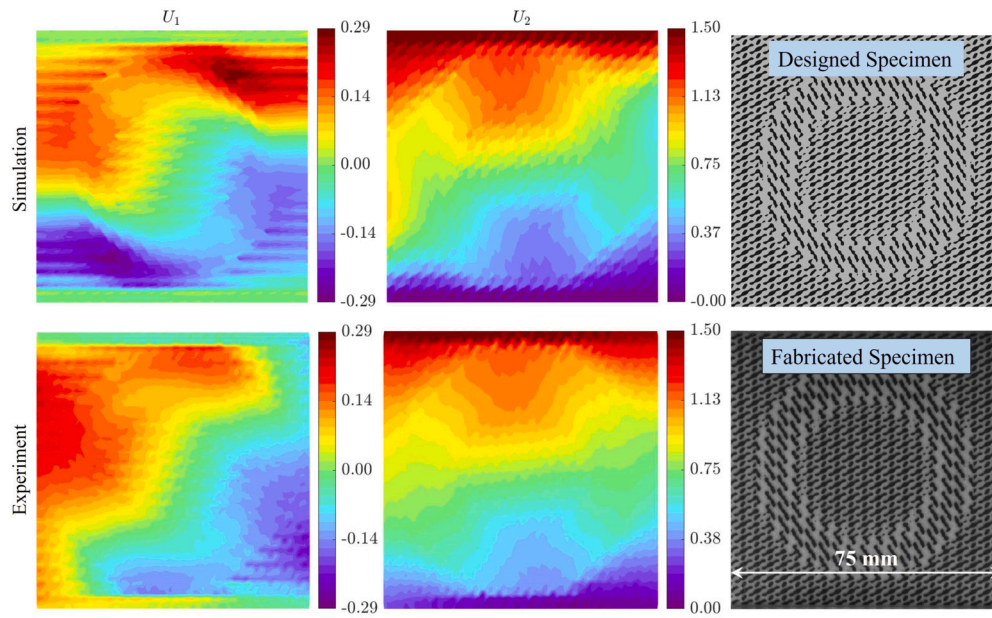
Fig. 8. Rotation-like deformation under tensile loading in a gradient structure made with annular interpolation. The prescribed displacement is 1.5 mm. The unit cell selection is discussed in Fig. S14. The geometric incompatibility between two unit cells with opposing shear-normal coupling behavior leads to non-affine deformation. The top row shows finite element simulation results while the bottom row shows the displacement contours measured using the digital image correlation (DIC) on an additively manufactured specimen.

coupling moduli. Additionally, experimentally measured strains are presented for this example in Fig. S16, indicating the localization of strain around the annular region.

Further, we explore the mechanical behavior of a tessellation obtained by repeating the supercell 4 × 4 times. We define the supercell as the entire annular interpolated structure shown in Fig. 8 with 20 × 20 unit cells. In Fig. 9, we plot the displacement and strain contours from the FEA on this supercell tessellation subjected to tensile loading by prescribing a displacement of 1.5 mm.[4] We observe that the non-affine rotation-like deformations induced by geometric frustration are present in this supercell tessellation at all the annular regions. Additionally, there is an observed gradient in this non-affine behavior in the horizontal displacement component (U_1). However, the magnitude of the horizontal displacement is reduced compared to the single supercell. There are non-local interactions from the neighboring annular regions. Similar behavior is observed in the case of supercell tessellation of example #2, as shown in Fig. S18. This suggests that the length scale as well as the separation between the annular regions play a significant role in affecting this rotation-like behavior, indicating the need to utilize micropolar elasticity in the context of such non-affine deformations in mechanical metamaterials [80].

In the future, a detailed investigation into this scale dependence could be conducted using a multi-scale homogenization approach. Further, it is interesting to note that when this structure is subjected to simple shear loading no distinct non-affine deformation is observed, as the unit cells don't differ in the shear-modulus like parameter C_{66}. Therefore, investigations on the role of incompatibilities in other moduli may unveil new insights into graded structures experiencing geometric frustration under other complex loading conditions. Finally, exploring other choices of unit cells with contrasting moduli interpolated nonlinearly could reveal unseen atypical mechanical behavior, which we leave for future work. In metallic materials with microstructure, defects such as grains and grain boundaries serve as strengthening mechanisms

by creating incompatibilities that obstruct simple deformation paths. For example, twin boundaries that arise when a sufficiently high shear load is applied, act as an energy dissipation mechanism contributing to the plasticity of various metals. Therefore, the nonlinear interpolations introduced in this work could be utilized to design strengthening mechanisms in metamaterials, notably for energy dissipation and impact loading, extending beyond lattice materials as discussed further in [81].

5. Conclusions

In this paper, we estimate the range of anisotropic stiffness tensors achieved by single-scale two-dimensional structured materials. We compare the property ranges reached by these single-scale architected materials with the extensive property space achieved by hierarchical laminates. In all property plots, we observed that rank-2 laminates significantly broaden the property range compared to rank-1 laminates. We identify regions in the property space, particularly focusing on off-axis shear-normal coupling parameters, where hierarchical designs or the use of two anisotropic constituent phases are necessary to cover a wide property space. The bounds estimated alongside the unit cell database could serve as a design tool for the design of extremal metamaterials. By utilizing unit cells with extreme anisotropy that lie on the property gamut boundary, we design and fabricate functionally graded metamaterials exhibiting behaviors such as energy localization and localized rotations. These behaviors are atypical to the corresponding boundary conditions, arising from incompatibilities in the deformation modes of the unit cells. We then established the concept of supercells which were created by tessellating an entire annular graded structure. In supercell designs, we observed that the annular regions displayed non-local interactions leading to length-scale dependent behavior.

Although our study primarily focused on exploring 2D linear elastic properties, the proposed method has the potential to estimate similar bounds for three-dimensional structured materials with shear-shear coupling. The diverse range of geometries compiled in our database could also prove useful for studying nonlinear phenomena such as dispersive wave propagation, and viscoelastic behavior in two-phase composites. Furthermore, the exploration of other supercell tessellations incorpo-
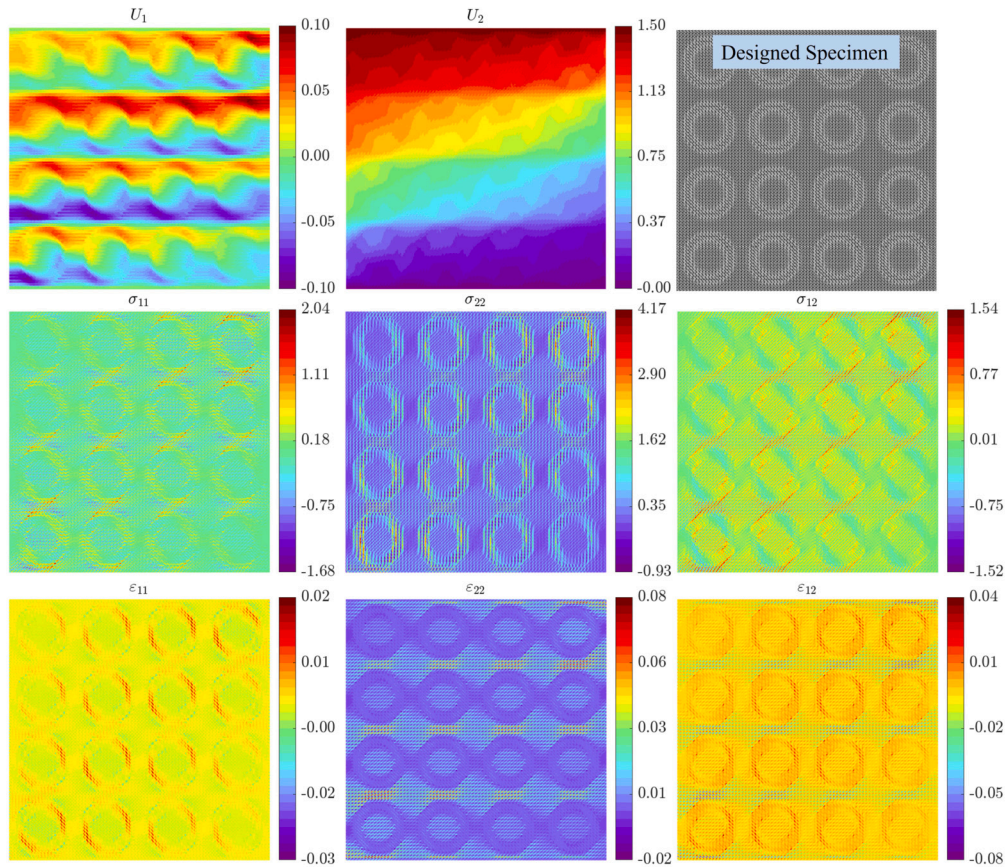
---

[4] Due to computational limitations, we limit our study to a 4 × 4 tessellation and reduce the unit cell size to 50 pixels from 100 pixels. For this 4 × 4 supercell tessellation, therefore, there are a total of $4 \times 4 \times 20 \times 20 = 6400$ unit cells resulting in a finite element mesh with $6400 \times 50 \times 50 = 16,000,000$ elements.

Fig. 9. Mechanical behavior in a 4×4 supercell tessellation design subjected to tensile loading. The supercell consists of unit cells with opposing shear-normal coupling arranged in an annular interpolation scheme, which is the entire specimen considered in Fig. 8. The displacement contour U_1 displays multiple regions of rotation-like deformation arising from incompatibilities in the deformation modes of the unit cells. σ_{11}, σ_{22} contours (in units of MPa) display how these incompatibilities in C_{16}, C_{26} lead to alternative regions of compressive and tensile stresses in the tessellated supercell undergoing tensile loading. σ_{12} contour shows the rotation-induced shear stress localization. All the strain contours further corroborate the localization of the strains around the annular interface.

rating different interpolation schemes could potentially open up new avenues in the design of multi-scale metamaterials and their nonlinear behavior.

CRediT authorship contribution statement

Jagannadh Boddapati: Writing – original draft, Visualization, Methodology, Investigation, Formal analysis, Conceptualization. **Chiara Daraio:** Writing – review & editing, Supervision, Funding acquisition, Conceptualization.

Declaration of competing interest

The authors declare that they have no known competing financial interests or personal relationships that could have appeared to influence the work reported in this paper.

Data availability

Data will be made available on request.

Acknowledgements

Appendix A. Database of elasticity tensors

A.1. Fourier analysis of pixelated geometries

Here, we justify the selection of cosine functions for unit cell database generation. Two unit cells are considered for comparison: the first unit cell is randomly generated, lacking distinctive patterns, and appearing almost noisy; the second is obtained using the method in Section 2. After Gaussian filtering, the Fourier spectrum of both unit cells is shown in Fig. A.10. To better illustrate the distribution of frequencies, the zero-frequency component, which represents the image's mean value and has the highest magnitude, is removed from the plots. For the almost noisy unit cell, the spectrum shows peaks across a wide range of spatial frequencies. In contrast, the second unit cell's spectrum is concentrated at lower spatial frequencies. This concentration justifies our choice of representation with very small spatial frequencies for generating the unit cells studied in this paper.

Further, in Table A.1, we compare the relation between four different exemplary function weights A_{mn} and the elastic tensor symmetries. Note that A_{00} corresponds to the central element of the matrix shown here. All the geometries are generated at a function threshold value of 0.6 and $\zeta = \max(m, n) = 2$. For Z_2 symmetry class, all the weights are entirely random. If the weights possess a plane of symmetry, like a diagonal symmetry $A_{mn} = A_{nm}$, it results in unit cells with D_2 symmetry. Similarly, if $A_{mn} = A_{-mn}$ (mirror symmetry in weights), it also results in D_2 symmetry. If the weights possess two planes of symmetry, $A_{mn} = A_{-mn}$ and $A_{mn} = A_{nm}$, it results in unit cells with D_4 symmetry. O_2 symmetry class requires use of rhombus-shaped unit cell (see [82].)
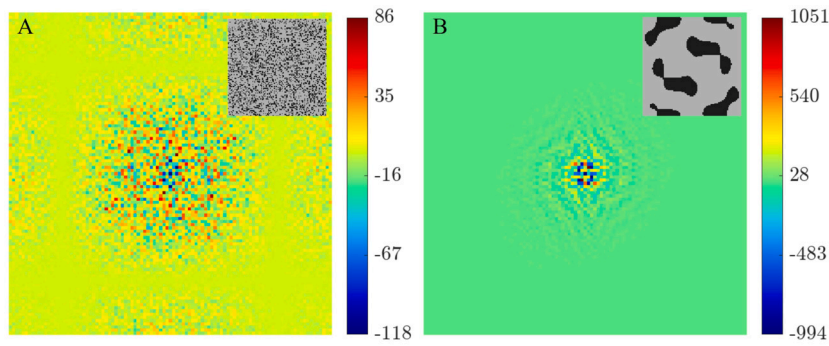
Fig. A.10. Fourier spectrum comparison of two different types of unit cells: (A) Inset shows a unit cell obtained as a random binary image with its corresponding real part of the Fourier spectrum. (B) Inset shows a unit cell obtained from the method described in Section 2 with its corresponding real part of the Fourier spectrum. Both the unit cells are chosen such that they have same fill fraction of the stiff phase.

Table A.1

Relation between four different exemplary function weights A_{mn} and the elastic tensor symmetries. All the geometries are generated with a function threshold value of 0.6 and $\zeta = \max(m, n) = 2$.

Function weights (A)	Geometry	Normalized Stiffness Tensor (C^H)	Symmetry Class
$\begin{bmatrix} 0.97 & 0.53 & 0.93 & 0.29 & -0.24 \\ 0.45 & -0.22 & 0.99 & -0.01 & -0.59 \\ -0.28 & -0.12 & 0.10 & 0.59 & -0.89 \\ 0.89 & -0.68 & -0.56 & 0.39 & 0.01 \\ -0.96 & -0.62 & -0.42 & -0.79 & 0.12 \end{bmatrix}$		$\begin{bmatrix} 0.19 & 0.08 & -0.05 \\ 0.08 & 1.05 & -0.06 \\ -0.05 & -0.06 & 0.06 \end{bmatrix}$	Z_2
$\begin{bmatrix} 0.05 & 0.42 & 0.05 & 0.33 & -0.66 \\ 0.42 & 0.11 & 0.01 & -0.45 & -0.15 \\ 0.05 & 0.01 & 0.48 & -0.01 & -0.78 \\ 0.33 & -0.45 & -0.01 & 0.60 & 0.53 \\ -0.66 & -0.15 & -0.78 & 0.53 & 0.88 \end{bmatrix}$		$\begin{bmatrix} 0.29 & 0.12 & -0.03 \\ 0.12 & 0.29 & -0.03 \\ -0.03 & -0.03 & 0.09 \end{bmatrix}$	D_2
$\begin{bmatrix} 0.41 & -0.37 & -0.02 & -0.37 & 0.41 \\ -0.65 & -0.73 & 0.87 & -0.73 & -0.65 \\ -0.18 & -0.02 & -0.41 & -0.025 & -0.18 \\ 0.17 & -0.78 & -0.29 & -0.78 & 0.17 \\ 0.12 & -0.04 & 0.53 & -0.04 & 0.12 \end{bmatrix}$		$\begin{bmatrix} 0.62 & 0.27 & 0.00 \\ 0.27 & 0.74 & 0.00 \\ 0.00 & 0.00 & 0.19 \end{bmatrix}$	D_2
$\begin{bmatrix} -0.01 & 0.18 & 0.200 & 0.18 & -0.01 \\ 0.18 & -0.15 & 0.03 & -0.15 & 0.18 \\ 0.20 & 0.03 & -0.15 & 0.0 & 0.20 \\ 0.18 & -0.15 & 0.03 & -0.15 & 0.18 \\ -0.01 & 0.18 & 0.20 & 0.18 & -0.01 \end{bmatrix}$		$\begin{bmatrix} 0.52 & 0.23 & 0.00 \\ 0.23 & 0.52 & 0.00 \\ 0.00 & 0.00 & 0.15 \end{bmatrix}$	D_4

A.2. Non-square unit cell data generation

In a 2D periodic system, the unit cells can be rectangular, square, parallelogram-shaped, or irregularly hexagonal. Using the concepts of Bravais lattices and Brillouin zone, it is sufficient to consider an arbitrary parallelogram-shaped unit cell defined by the side lengths a, b and the angle between the edges $90° - \theta$, to describe all possible unit cell shapes completely [82]. The values for parallelogram $a = 1, b = 1, \theta = 30°$ would give an equivalent regular hexagonal unit cell. Therefore, to generate non-square unit cell data, we considered several non-square oblique unit cells when the angle parameter is varied such that $-45° < \theta < 45°$, while the ratio of side length is varied such that $0.3 \leq \frac{a}{b} \leq 3$.

A.3. Theory of bounds on anisotropic elasticity tensors

For isotropic composites, Hashin and Shtrikman [37,38] introduced a variational approach to determine the upper and lower bounds on the effective bulk and shear moduli (κ^* and μ^*) by decomposing the elastic energy into hydrostatic and deviatoric parts. However, the elastic energy

cannot be decomposed to obtain variational bounds on the independent moduli in the anisotropic case. Recently Milton et al. [84] and Milton and Camar-Eddine [43] addressed this problem in terms of the stress and strain energy pairs and establishing bounds on the sum of the elastic and the complementary energies. Let the four energy functions $W_f^k, k = 0, 1, \ldots, 3$, that characterize the set GU_f of possible elastic tensors C_* be defined by

$$W_f^0 \left(\sigma_1^0, \sigma_2^0, \sigma_3^0 \right) = \min_{C_* \in GU_f} \sum_{j=1}^{3} \sigma_j^0 : C_*^{-1} \sigma_j^0, \tag{A.1a}$$

$$W_f^1 \left(\sigma_1^0, \sigma_2^0, \varepsilon_1^0 \right) = \min_{C_* \in GU_f} \left[\varepsilon_1^0 : C_* \varepsilon_1^0 + \sum_{j=1}^{2} \sigma_j^0 : C_*^{-1} \sigma_j^0 \right], \tag{A.1b}$$

$$W_f^2 \left(\sigma_1^0, \varepsilon_1^0, \varepsilon_2^0 \right) = \min_{C_* \in GU_f} \left[\left(\sum_{i=1}^{2} \varepsilon_i^0 : C_* \varepsilon_i^0 \right) + \sigma_1^0 : C_*^{-1} \sigma_1^0 \right], \tag{A.1c}$$

$$W_f^3 \left(\varepsilon_1^0, \varepsilon_2^0, \varepsilon_3^0 \right) = \min_{C_* \in GU_f} \sum_{i=1}^{3} \varepsilon_i^0 : C_* \varepsilon_i^0. \tag{A.1d}$$
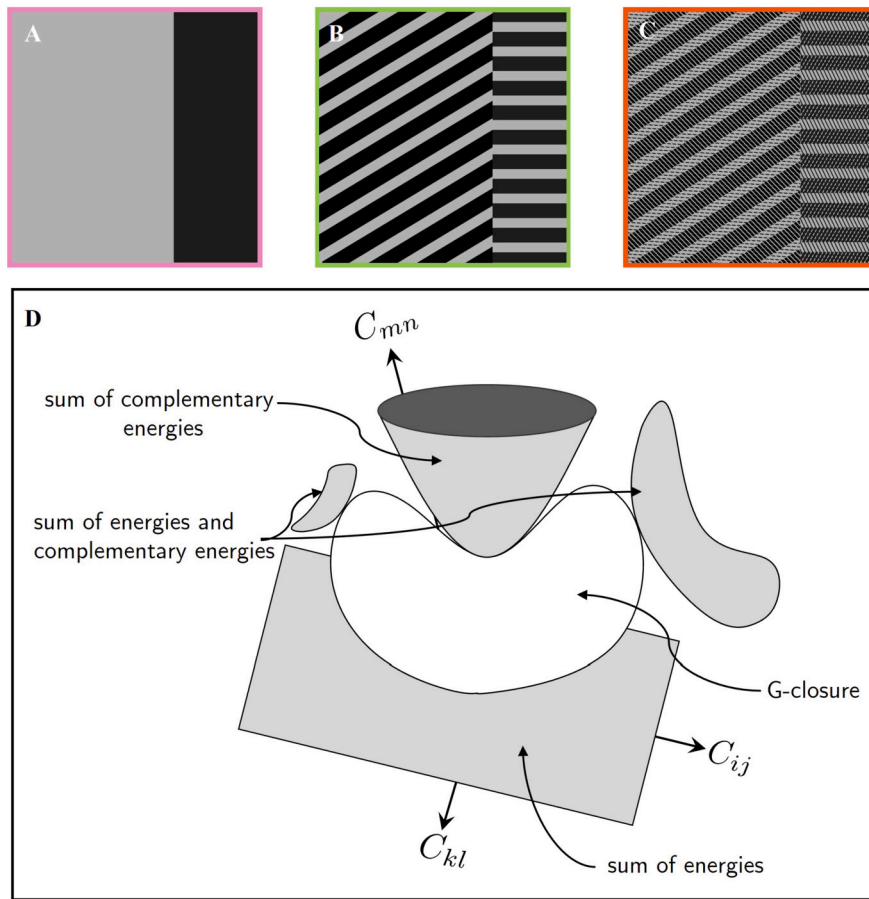
Fig. A.11. (A,B,C) Construction of hierarchical laminates of rank-1, rank-2 and rank-3 respectively. For rank-2 laminates, the stiff and soft phases of rank-1 are further laminated in an arbitrarily chosen direction, not necessarily identical to the lamination direction of the rank-1 laminate. Similarly for rank-3 laminates, each rank-1 lamination in rank-2 laminate is laminated again in arbitrary directions. The fill fraction and relative orientation in each sequence of hierarchy are fixed to show the distinction of hierarchy. (D) G-closures are defined by the minimum values of sums of energies and complementary energies. The coordinates represent components of the elasticity tensor. The convexity of the G-closure ensures that the surfaces of energies and complementary energies touch every point tangentially on its boundary (adapted and redrawn from Figure 30.1 in [83]). Further, it has been shown that the composites that lie on the boundary of this G-closure are usually hierarchical laminates.

Each energy function $W_f^k, k = 0, 1, \dots, 3$, here represents the sum of three elastic energies, each obtained from an experiment where the composite, with effective tensor $\mathbf{C}_*$, is either subject to an applied stress σ_i^0 or an applied strain ε_i^0. A total of three stresses σ_i^0 and ε_i^0 are applied simultaneously on the composite. The optimization of these energies to find $\mathbf{C}_*$ for the applied stresses and strains is non-trivial. However, applying the key conclusions from [39,42,85], Milton and Camar-Eddine [43], Milton et al. [84] discuss how sequentially layered laminates (or hierarchical laminates) minimize the sum of energies and complementary energies. In other words, G-closure can be seen as the G-closure of hierarchical laminates which is explained in Fig. A.11. In two-dimensions, it is sufficient to consider laminates up to rank-3, if the constituent phases are isotropic. It is also worth noting that hierarchical laminates, with isotropic type effective elasticity tensor, simultaneously achieve Hashin-Shtrikman bulk and shear bounds [57].

A.4. Construction of hierarchical laminates

Multiple-rank laminate materials are hierarchical materials created through an iterative lamination process at increasingly larger length scales. A rank-one laminate consists of two isotropic phases, which can be viewed as rank-zero laminates. A rank-(m) laminate is formed by layering a rank-($m-1$) laminate with a laminate of rank-($m-1$) or lower, as shown in Fig. A.11. In two dimensions, it is sufficient to consider laminates up to rank-3 to estimate theoretical bounds, especially

when the constituent materials are isotropic, as the 2D elasticity tensor has only three eigenvalues. Rank-1 laminates typically have one very high non-zero eigenvalue and two near-zero eigenvalues, while rank-2 laminates have two very high non-zero eigenvalues and one near-zero eigenvalue. To compute the effective properties of a higher rank-m laminate, the constituent phases are replaced from isotropic to the relevant anisotropic phases of rank-($m-1$) laminates (see Figs. S5 to S7). A rank-1 laminate is strictly defined by two parameters, the fill fraction of the stiff phase and the angle of orientation of the lamination. A rank-2 laminate is defined by four extra parameters the fill fraction of the stiff phase and the angle of orientation of each of the phases of the previous rank-1 laminate. Similarly, a rank-3 laminate is defined by eight extra parameters. Suppose, there are 11 different fill fractions and 18 different laminate orientations. This results in a total of $11 \times 18 = 198$ elasticity tensors for rank-1 laminates. For rank-2 laminates, the total number of possible elasticity tensors is $(11 \times 18)^3 = 7762392$. For rank-3 laminates, the number increases to $(11 \times 18)^7$. First, the effective properties of all the rank-1 laminates are obtained by using two isotropic constituent phases for homogenization. To compute the effective properties of higher rank-m laminates, the constituent phases are replaced from isotropic to the relevant anisotropic phases of lower rank (see Fig. S5 to S7). To reduce the number of computations for the rank-3 laminates database, a subset of randomly chosen rank-2 elasticity tensors (about 1%) are used.

Appendix B. Supplementary material

Supplementary material related to this article can be found online at https://doi.org/10.1016/j.matdes.2024.113348.

References

[1] J.U. Surjadi, L. Gao, H. Du, X. Li, X. Xiong, N.X. Fang, Y. Lu, Mechanical metamaterials and their engineering applications, Adv. Eng. Mater. 21 (2019) 1800864, https://doi.org/10.1002/adem.201800864, https://onlinelibrary.wiley.com/doi/pdf/10.1002/adem.201800864.

[2] K.K. Saxena, R. Das, E.P. Calius, Three decades of auxetics research - materials with negative Poisson's ratio: a review, Adv. Eng. Mater. 18 (2016) 1847–1870, https://doi.org/10.1002/adem.201600053, https://onlinelibrary.wiley.com/doi/pdf/10.1002/adem.201600053.

[3] J. Panetta, Q. Zhou, L. Malomo, N. Pietroni, P. Cignoni, D. Zorin, Elastic textures for additive fabrication, ACM Trans. Graph. 34 (2015) 1–12, https://doi.org/10.1145/2766937, https://dl.acm.org/doi/10.1145/2766937.

[4] C. Schumacher, B. Bickel, J. Rys, S. Marschner, C. Daraio, M. Gross, Microstructures to control elasticity in 3D printing, ACM Trans. Graph. 34 (2015) 1–13, https://doi.org/10.1145/2766926, https://dl.acm.org/doi/10.1145/2766926.

[5] T. Bückmann, M. Thiel, M. Kadic, R. Schittny, M. Wegener, An elasto-mechanical unfeelability cloak made of pentamode metamaterials, Nat. Commun. 5 (2014) 4130, https://doi.org/10.1038/ncomms5130, https://www.nature.com/articles/ncomms5130, number: 1, Publisher: Nature Publishing Group.

[6] L. Wang, J. Boddapati, K. Liu, P. Zhu, C. Daraio, W. Chen, Mechanical cloak via data-driven aperiodic metamaterial design, Proc. Natl. Acad. Sci. 119 (2022) e2122185119, https://doi.org/10.1073/pnas.2122185119, https://pnas.org/doi/full/10.1073/pnas.2122185119.

[7] K. Gupta, K. Meena, Artificial bone scaffolds and bone joints by additive manufacturing: a review, Bioprinting 31 (2023) e00268, https://doi.org/10.1016/j.bprint.2023.e00268, https://www.sciencedirect.com/science/article/pii/S2405886623000118.

[8] W. Wu, X. Song, J. Liang, R. Xia, G. Qian, D. Fang, Mechanical properties of anti-tetrachiral auxetic stents, Compos. Struct. 185 (2018) 381–392, https://doi.org/10.1016/j.compstruct.2017.11.048, https://www.sciencedirect.com/science/article/pii/S0263822317324078.

[9] S. Oh, T.E. Song, M. Mahato, J.S. Kim, H. Yoo, M.J. Lee, M. Khan, W.H. Yeo, I.K. Oh, Easy-to-wear auxetic SMA knot-architecture for spatiotemporal and multimodal haptic feedbacks, Adv. Mater. 35 (2023) 2304442, https://doi.org/10.1002/adma.202304442, https://onlinelibrary.wiley.com/doi/pdf/10.1002/adma.202304442.

[10] J. Lee, Y.Y. Kim, Elastic metamaterials for guided waves: from fundamentals to applications, Smart Mater. Struct. 32 (2023) 123001, https://doi.org/10.1088/1361-665X/ad0393, https://dx.doi.org/10.1088/1361-665X/ad0393, publisher: IOP Publishing.

[11] L.J. Gibson, M.F. Ashby, Cellular Solids: Structure and Properties, 2 ed., Cambridge Solid State Science Series, Cambridge University Press, Cambridge, 1997, https://www.cambridge.org/core/books/cellular-solids/BC25789552BAA8E3CAD5E1D105612AB5.

[12] N.A. Fleck, V.S. Deshpande, M.F. Ashby, Micro-architectured materials: past, present and future, Proc. R. Soc. A, Math. Phys. Eng. Sci. 466 (2010) 2495–2516, https://doi.org/10.1098/rspa.2010.0215, https://royalsocietypublishing.org/doi/full/10.1098/rspa.2010.0215, publisher: Royal Society.

[13] C. Soyarslan, S. Bargmann, M. Pradas, J. Weissmüller, 3D stochastic bicontinuous microstructures: generation, topology and elasticity, Acta Mater. 149 (2018) 326–340, https://doi.org/10.1016/j.actamat.2018.01.005, https://www.sciencedirect.com/science/article/pii/S1359645418300363.

[14] N. Karathanasopoulos, F. Dos Reis, M. Diamantopoulou, J.F. Ganghoffer, Mechanics of beams made from chiral metamaterials: tuning deflections through normal-shear strain couplings, Mater. Des. 189 (2020) 108520, https://doi.org/10.1016/j.matdes.2020.108520, https://www.sciencedirect.com/science/article/pii/S0264127520300538.

[15] F. Agnelli, G. Nika, A. Constantinescu, Design of thin micro-architectured panels with extension–bending coupling effects using topology optimization, Comput. Methods Appl. Mech. Eng. 391 (2022) 114496, https://doi.org/10.1016/j.cma.2021.114496, https://www.sciencedirect.com/science/article/pii/S0045782521007040.

[16] W. Lee, J. Lee, C.I. Park, Y.Y. Kim, Polarization-independent full mode-converting elastic metasurfaces, Int. J. Mech. Sci. 266 (2024) 108975, https://doi.org/10.1016/j.ijmecsci.2024.108975, https://www.sciencedirect.com/science/article/pii/S0020740324000183.

[17] S. Tomita, K. Shimanuki, S. Oyama, H. Nishigaki, T. Nakagawa, M. Tsutsui, Y. Emura, M. Chino, H. Tanaka, Y. Itou, K. Umemoto, Transition of deformation modes from bending to auxetic compression in origami-based metamaterials for head protection from impact, Sci. Rep. 13 (2023) 12221, https://doi.org/10.1038/s41598-023-39200-8, https://www.nature.com/articles/s41598-023-39200-8, publisher: Nature Publishing Group.

[18] X. Liu, G. Hu, Elastic metamaterials making use of chirality: a review. Strojniški vestnik, J. Mech. Eng. 62 (2016) 403–418, https://doi.org/10.5545/sv-jme.2016.3799, http://www.sv-jme.eu/article/elastic-metamaterials-making-use-of-chirality-a-review/.

[19] O. Sigmund, Systematic design of metamaterials by topology optimization, in: R. Pyrz, J.C. Rauhe (Eds.), IUTAM Symposium on Modelling Nanomaterials and Nanosystems, Springer, Netherlands, Dordrecht, 2009, pp. 151–159.

[20] A.R. Diaz, A. Bénard, Designing materials with prescribed elastic properties using polygonal cells, Int. J. Numer. Methods Eng. 57 (2003) 301–314, https://doi.org/10.1002/nme.677, https://onlinelibrary.wiley.com/doi/pdf/10.1002/nme.677.

[21] I. Ostanin, G. Ovchinnikov, D.C. Tozoni, D. Zorin, A parametric class of composites with a large achievable range of effective elastic properties, J. Mech. Phys. Solids 118 (2018) 204–217, https://doi.org/10.1016/j.jmps.2018.05.018, https://www.sciencedirect.com/science/article/pii/S0022509617311183.

[22] T.S. Lumpe, T. Stankovic, Exploring the property space of periodic cellular structures based on crystal networks, Proc. Natl. Acad. Sci. 118 (2021) e2003504118, https://doi.org/10.1073/pnas.2003504118, https://pnas.org/doi/full/10.1073/pnas.2003504118.

[23] S. Luan, E. Chen, J. John, S. Gaitanaros, A data-driven framework for structure-property correlation in ordered and disordered cellular metamaterials, Sci. Adv. 9 (2023) eadi1453, https://doi.org/10.1126/sciadv.adi1453, https://www.science.org/doi/10.1126/sciadv.adi1453, publisher: American Association for the Advancement of Science.

[24] Z. Zhang, C. Brandt, J. Jouve, Y. Wang, T. Chen, M. Pauly, J. Panetta, Computational design of flexible planar microstructures, ACM Trans. Graph. 42 (2023) 1–16, https://doi.org/10.1145/3618396, https://dl.acm.org/doi/10.1145/3618396.

[25] D. Chen, M. Skouras, B. Zhu, W. Matusik, Computational discovery of extremal microstructure families, Sci. Adv. 4 (2018) eaao7005, https://doi.org/10.1126/sciadv.aao7005, https://www.science.org/doi/10.1126/sciadv.aao7005.

[26] X. Zheng, X. Zhang, T.T. Chen, I. Watanabe, Deep learning in mechanical metamaterials: from prediction and generation to inverse design, Adv. Mater. 35 (2023) 2302530, https://doi.org/10.1002/adma.202302530, https://onlinelibrary.wiley.com/doi/abs/10.1002/adma.202302530.

[27] D. Lee, W.W. Chen, L. Wang, Y.C. Chan, W. Chen, Data-driven design for metamaterials and multiscale systems: a review, Adv. Mater. 36 (2024) 2305254, https://doi.org/10.1002/adma.202305254, https://onlinelibrary.wiley.com/doi/pdf/10.1002/adma.202305254.

[28] L. Wang, Y.C. Chan, F. Ahmed, Z. Liu, P. Zhu, W. Chen, Deep generative modeling for mechanistic-based learning and design of metamaterial systems, Comput. Methods Appl. Mech. Eng. 372 (2020) 113377, https://doi.org/10.1016/j.cma.2020.113377, https://www.sciencedirect.com/science/article/pii/S0045782520305624.

[29] Y. Mao, Q. He, X. Zhao, Designing complex architectured materials with generative adversarial networks, Sci. Adv. 6 (2020) eaaz4169, https://doi.org/10.1126/sciadv.aaz4169, https://www.science.org/doi/10.1126/sciadv.aaz4169.

[30] S. Kumar, S. Tan, L. Zheng, D.M. Kochmann, Inverse-designed spinodoid metamaterials, npj Comput. Mater. 6 (2020) 73, https://doi.org/10.1038/s41524-020-0341-6, http://www.nature.com/articles/s41524-020-0341-6.

[31] J.H. Bastek, S. Kumar, B. Telgen, R.N. Glaesener, D.M. Kochmann, Inverting the structure–property map of truss metamaterials by deep learning, Proc. Natl. Acad. Sci. 119 (2022) e2111505119, https://doi.org/10.1073/pnas.2111505119, https://www.pnas.org/doi/abs/10.1073/pnas.2111505119, publisher: Proceedings of the National Academy of Sciences.

[32] L. Zheng, K. Karapiperis, S. Kumar, D.M. Kochmann, Unifying the design space and optimizing linear and nonlinear truss metamaterials by deep learning, Nat. Commun. 14 (2023) 7563, https://doi.org/10.1038/s41467-023-42068-x, https://www.nature.com/articles/s41467-023-42068-x, number: 1, publisher: Nature Publishing Group.

[33] C. Yang, Y. Kim, S. Ryu, G.X. Gu, Using convolutional neural networks to predict composite properties beyond the elastic limit, MRS Commun. 9 (2019) 609–617, https://doi.org/10.1557/mrc.2019.49, https://www.cambridge.org/core/journals/mrs-communications/article/using-convolutional-neural-networks-to-predict-composite-properties-beyond-the-elastic-limit/D58F4D59C1644EEB704B07D04F0CE220, publisher: Cambridge University Press.

[34] M. Maurizi, C. Gao, F. Berto, Inverse design of truss lattice materials with superior buckling resistance, npj Comput. Mater. 8 (2022) 1–12, https://doi.org/10.1038/s41524-022-00938-w, https://www.nature.com/articles/s41524-022-00938-w, number: 1, publisher: Nature Publishing Group.

[35] J.H. Bastek, D.M. Kochmann, Inverse design of nonlinear mechanical metamaterials via video denoising diffusion models, Nat. Mach. Intell. 5 (2023) 1466–1475, https://doi.org/10.1038/s42256-023-00762-x, https://www.nature.com/articles/s42256-023-00762-x, number: 12, Publisher: Nature Publishing Group.

[36] G.W. Milton, Some open problems in the theory of composites, Philos. Trans. - Royal Soc., Math. Phys. Eng. Sci. 379 (2021) 20200115, https://doi.org/10.1098/rsta.2020.0115, https://royalsocietypublishing.org/doi/10.1098/rsta.2020.0115, publisher: Royal Society.

[37] Z. Hashin, S. Shtrikman, Note on a variational approach to the theory of composite elastic materials, J. Franklin Inst. 271 (1961) 336–341, https://doi.org/10.1016/0016-0032(61)90032-1, https://linkinghub.elsevier.com/retrieve/pii/0016003261900321.

[38] Z. Hashin, S. Shtrikman, On some variational principles in anisotropic and nonhomogeneous elasticity, J. Mech. Phys. Solids 10 (1962) 335–342, https://doi.org/10.1016/0022-5096(62)90004-2, https://www.sciencedirect.com/science/article/pii/0022509662900042.

[39] J.R. Willis, Bounds and self-consistent estimates for the overall properties of anisotropic composites, J. Mech. Phys. Solids 25 (1977) 185–202, https://doi.org/10.1016/0022-5096(77)90022-9, https://www.sciencedirect.com/science/article/pii/0022509677900229.

[40] G.W. Milton, R.V. Kohn, Variational bounds on the effective moduli of anisotropic composites, J. Mech. Phys. Solids 36 (1988) 597–629, https://doi.org/10.1016/0022-5096(88)90001-4, https://www.sciencedirect.com/science/article/pii/0022509688900014.

[41] A.V. Cherkaev, L.V. Gibiansky, Coupled estimates for the bulk and shear moduli of a two-dimensional isotropic elastic composite, J. Mech. Phys. Solids 41 (1993) 937–980, https://doi.org/10.1016/0022-5096(93)90006-2, https://www.sciencedirect.com/science/article/pii/0022509693900062.

[42] G. Allaire, R.V. Kohn, Optimal bounds on the effective behavior of a mixture of two well-ordered elastic materials, Q. Appl. Math. 51 (1993) 643–674, https://doi.org/10.1090/qam/1247433, https://www.ams.org/qam/1993-51-04/S0033-569X-1993-1247433-7/.

[43] G.W. Milton, M. Camar-Eddine, Near optimal pentamodes as a tool for guiding stress while minimizing compliance in 3d-printed materials: a complete solution to the weak G-closure problem for 3d-printed materials, J. Mech. Phys. Solids 114 (2018) 194–208, https://doi.org/10.1016/j.jmps.2018.02.003, https://www.sciencedirect.com/science/article/pii/S0022509617310967.

[44] G.W. Milton, A.V. Cherkaev, Which elasticity tensors are realizable?, J. Eng. Mater. Technol. 117 (1995) 483–493, https://doi.org/10.1115/1.2804743.

[45] Z. Wei, Z. Hu, R. Zhu, Y. Chen, G. Hu, A transformable anisotropic 3D penta-mode metamaterial, Mater. Des. 234 (2023) 112306, https://doi.org/10.1016/j.matdes.2023.112306, https://www.sciencedirect.com/science/article/pii/S0264127523007219.

[46] O. Sigmund, A new class of extremal composites, J. Mech. Phys. Solids 48 (2000) 397–428, https://doi.org/10.1016/S0022-5096(99)00034-4, https://www.sciencedirect.com/science/article/pii/S0022509699000344.

[47] Z. Hu, Z. Wei, K. Wang, Y. Chen, R. Zhu, G. Huang, G. Hu, Engineering zero modes in transformable mechanical metamaterials, Nat. Commun. 14 (2023) 1266, https://doi.org/10.1038/s41467-023-36975-2, https://www.nature.com/articles/s41467-023-36975-2, number: 1, publisher: Nature Publishing Group.

[48] A. Freidin, On new phase inclusions in elastic solids, Z. Angew. Math. Mech. 87 (2007) 102–116, https://doi.org/10.1002/zamm.200610305, https://onlinelibrary.wiley.com/doi/10.1002/zamm.200610305.

[49] I.V. Chenchiah, K. Bhattacharya, The relaxation of two-well energies with possibly unequal moduli, Arch. Ration. Mech. Anal. 187 (2008) 409–479, https://doi.org/10.1007/s00205-007-0075-3.

[50] M.A. Antimonov, A. Cherkaev, A.B. Freidin, Phase transformations surfaces and exact energy lower bounds, Int. J. Eng. Sci. 98 (2016) 153–182, https://doi.org/10.1016/j.ijengsci.2015.10.004, https://linkinghub.elsevier.com/retrieve/pii/S0020722515001408.

[51] A.B. Freidin, L.L. Sharipova, Two-phase equilibrium microstructures against optimal composite microstructures, Arch. Appl. Mech. 89 (2019) 561–580, https://doi.org/10.1007/s00419-019-01510-7, http://link.springer.com/10.1007/s00419-019-01510-7.

[52] G.A. Francfort, G.W. Milton, Sets of conductivity and elasticity tensors stable under lamination, Commun. Pure Appl. Math. 47 (1994) 257–279, https://doi.org/10.1002/cpa.3160470302, https://onlinelibrary.wiley.com/doi/pdf/10.1002/cpa.3160470302.

[53] J. Boddapati, M. Flaschel, S. Kumar, L. De Lorenzis, C. Daraio, Single-test evaluation of directional elastic properties of anisotropic structured materials, J. Mech. Phys. Solids 181 (2023) 105471, https://doi.org/10.1016/j.jmps.2023.105471, https://www.sciencedirect.com/science/article/pii/S0022509623002752.

[54] J.W. Cahn, Phase separation by spinodal decomposition in isotropic systems, J. Chem. Phys. 42 (1965) 93–99, https://doi.org/10.1063/1.1695731, https://pubs.aip.org/jcp/article/42/1/93/81515/Phase-Separation-by-Spinodal-Decomposition-in.

[55] D. Zhang, G. Lu, Shape-based image retrieval using generic Fourier descriptor, Signal Process. Image Commun. 17 (2002) 825–848, https://doi.org/10.1016/S0923-5965(02)00084-X, https://www.sciencedirect.com/science/article/pii/S092359650200084X.

[56] S. Yu, Y. Zhang, C. Wang, W.k. Lee, B. Dong, T.W. Odom, C. Sun, W. Chen, Characterization and design of functional quasi-random nanostructured materials using spectral density function, J. Mech. Des. 139 (2017) 071401, https://doi.org/10.1115/1.4036582, https://asmedigitalcollection.asme.org/mechanicaldesign/article/doi/10.1115/1.4036582/383763/Characterization-and-Design-of-Functional.

[57] G.A. Francfort, F. Murat, Homogenization and optimal bounds in linear elasticity, Arch. Ration. Mech. Anal. 94 (1986) 307–334, https://doi.org/10.1007/BF00280908.

[58] E. Andreassen, C.S. Andreasen, How to determine composite material properties using numerical homogenization, Comput. Mater. Sci. 83 (2014) 488–495, https://doi.org/10.1016/j.commatsci.2013.09.006, https://www.sciencedirect.com/science/article/pii/S0927025613005302.

[59] D. Nepal, S. Kang, K.M. Adstedt, K. Kanhaiya, M.R. Bockstaller, L.C. Brinson, M.J. Buehler, P.V. Coveney, K. Dayal, J.A. El-Awady, L.C. Henderson, D.L. Kaplan, S. Keten, N.A. Kotov, G.C. Schatz, S. Vignolini, F. Vollrath, Y. Wang, B.I. Yakobson, V.V. Tsukruk, H. Heinz, Hierarchically structured bioinspired nanocomposites, Nat. Mater. 22 (2023) 18–35, https://doi.org/10.1038/s41563-022-01384-1, https://www.nature.com/articles/s41563-022-01384-1, publisher: Nature Publishing Group.

[60] K. Feyrer, Wire Ropes, Springer, Berlin, Heidelberg, 2007, http://link.springer.com/10.1007/978-3-540-33831-4.

[61] J. Tavakoli, J.J. Costi, Ultrastructural organization of elastic fibres in the partition boundaries of the annulus fibrosus within the intervertebral disc, Acta Biomater. 68 (2018) 67–77, https://doi.org/10.1016/j.actbio.2017.12.017, https://www.sciencedirect.com/science/article/pii/S1742706117307833.

[62] G. Volandri, F. Di Puccio, P. Forte, C. Carmignani, Biomechanics of the tympanic membrane, J. Biomech. 44 (2011) 1219–1236, https://doi.org/10.1016/j.jbiomech.2010.12.023, https://www.sciencedirect.com/science/article/pii/S0021929011000224.

[63] S. Forte, M. Vianello, A unified approach to invariants of plane elasticity tensors, Meccanica 49 (2014) 2001–2012, https://doi.org/10.1007/s11012-014-9916-y, http://link.springer.com/10.1007/s11012-014-9916-y.

[64] B. Liu, X. Feng, S.M. Zhang, The effective Young's modulus of composites beyond the Voigt estimation due to the Poisson effect, Compos. Sci. Technol. 69 (2009) 2198–2204, https://doi.org/10.1016/j.compscitech.2009.06.004, https://www.sciencedirect.com/science/article/pii/S0266353809002218.

[65] H. Niknam, A.H. Akbarzadeh, Graded lattice structures: simultaneous enhancement in stiffness and energy absorption, Mater. Des. 196 (2020) 109129, https://doi.org/10.1016/j.matdes.2020.109129, https://www.sciencedirect.com/science/article/pii/S026412752030664X.

[66] D. Chen, K. Gao, J. Yang, L. Zhang, Functionally graded porous structures: analyses, performances, and applications – a review, Thin-Walled Struct. 191 (2023) 111046, https://doi.org/10.1016/j.tws.2023.111046, https://www.sciencedirect.com/science/article/pii/S0263823123005244.

[67] A. Panesar, M. Abdi, D. Hickman, I. Ashcroft, Strategies for functionally graded lattice structures derived using topology optimisation for additive manufacturing, Addit. Manuf. 19 (2018) 81–94, https://doi.org/10.1016/j.addma.2017.11.008, https://www.sciencedirect.com/science/article/pii/S221486041730115X.

[68] E.D. Sanders, A. Pereira, G.H. Paulino, Optimal and continuous multilattice embedding, Sci. Adv. 7 (2021) eabf4838, https://doi.org/10.1126/sciadv.abf4838, https://www.science.org/doi/10.1126/sciadv.abf4838, publisher: American Association for the Advancement of Science.

[69] Y. Wang, L. Zhang, S. Daynes, H. Zhang, S. Feih, M.Y. Wang, Design of graded lattice structure with optimized mesostructures for additive manufacturing, Mater. Des. 142 (2018) 114–123, https://doi.org/10.1016/j.matdes.2018.01.011, https://www.sciencedirect.com/science/article/pii/S026412751830011X.

[70] H. Li, Z. Luo, L. Gao, P. Walker, Topology optimization for functionally graded cellular composites with metamaterials by level sets, Comput. Methods Appl. Mech. Eng. 328 (2018) 340–364, https://doi.org/10.1016/j.cma.2017.09.008, https://www.sciencedirect.com/science/article/pii/S0045782516310106.

[71] E. Garner, H.M.A. Kolken, C.C.L. Wang, A.A. Zadpoor, J. Wu, Compatibility in microstructural optimization for additive manufacturing, Addit. Manuf. 26 (2019) 65–75, https://doi.org/10.1016/j.addma.2018.12.007, https://www.sciencedirect.com/science/article/pii/S2214860418306808.

[72] G. Lee, S.J. Lee, J. Rho, M. Kim, Acoustic and mechanical metamaterials for energy harvesting and self-powered sensing applications, Mater. Today Energy 37 (2023) 101387, https://doi.org/10.1016/j.mtener.2023.101387, https://www.sciencedirect.com/science/article/pii/S2468606923001430.

[73] G. Lee, D. Lee, J. Park, Y. Jang, M. Kim, J. Rho, Piezoelectric energy harvesting using mechanical metamaterials and phononic crystals, Commun. Phys. 5 (2022) 1–16, https://doi.org/10.1038/s42005-022-00869-4, https://www.nature.com/articles/s42005-022-00869-4, publisher: Nature Publishing Group.

[74] M. Rubinstein, S. Panyukov, Nonaffine deformation and elasticity of polymer networks, Macromolecules 30 (1997) 8036–8044, https://doi.org/10.1021/ma970364k, publisher: American Chemical Society.

[75] W.G. Ellenbroek, Z. Zeravcic, W.v. Saarloos, M.v. Hecke, Non-affine response: jammed packings vs. spring networks, Europhys. Lett. 87 (2009) 34004, https://doi.org/10.1209/0295-5075/87/34004, https://dx.doi.org/10.1209/0295-5075/87/34004.

[76] H. Schreier, J.J. Orteu, M.A. Sutton, Image Correlation for Shape, Motion and Deformation Measurements: Basic Concepts, Theory and Applications, Springer US, Boston, MA, 2009, https://link.springer.com/10.1007/978-0-387-78747-3.

[77] F. Hild, S. Roux, Comparison of local and global approaches to digital image correlation, Exp. Mech. 52 (2012) 1503–1519, https://doi.org/10.1007/s11340-012-9603-7.

[78] F. Agnelli, P. Margerit, P. Celli, C. Daraio, A. Constantinescu, Systematic two-scale image analysis of extreme deformations in soft architectured sheets, Int. J. Mech. Sci. 194 (2021) 106205, https://doi.org/10.1016/j.ijmecsci.2020.106205, https://www.sciencedirect.com/science/article/pii/S0020740320343101.

[79] N. Levy, P.V. Marcal, J.R. Rice, Progress in three-dimensional elastic-plastic stress analysis for fracture mechanics, Nucl. Eng. Des. 17 (1971) 64–75, https://doi.org/10.1016/0029-5493(71)90040-9, https://www.sciencedirect.com/science/article/pii/0029549371900409.

[80] B. Lemkalli, M. Kadic, Y. El Badri, S. Guenneau, A. Bouzid, Y. Achaoui, Mapping of elastic properties of twisting metamaterials onto micropolar continuum using static calculations, Int. J. Mech. Sci. 254 (2023) 108411, https://doi.org/10.1016/j.ijmecsci.2023.108411, https://www.sciencedirect.com/science/article/pii/S0020740323003132.

[81] M.S. Pham, C. Liu, I. Todd, J. Lertthanasarn, Damage-tolerant architected materials inspired by crystal microstructure, Nature 565 (2019) 305–311, https://doi.org/10.1038/s41586-018-0850-3, https://www.nature.com/articles/s41586-018-0850-3, publisher: Nature Publishing Group.

[82] J. Podestá, C. Méndez, S. Toro, A. Huespe, Symmetry considerations for topology design in the elastic inverse homogenization problem, J. Mech. Phys. Solids 128 (2019) 54–78, https://doi.org/10.1016/j.jmps.2019.03.018, https://linkinghub.elsevier.com/retrieve/pii/S0022509618305210.

[83] G.W. Milton, Chapter 30: properties of the G-closure and extremal families of composites, in: The Theory of Composites, in: Classics in Applied Mathematics, Society for Industrial and Applied Mathematics, 2022, pp. 643–669, https://epubs.siam.org/doi/10.1137/1.9781611977486.ch30.

[84] G. Milton, M. Briane, D. Harutyunyan, On the possible effective elasticity tensors of 2-dimensional and 3-dimensional printed materials, Math. Mech. Complex Syst. 5 (2017) 41–94, https://doi.org/10.2140/memocs.2017.5.41, http://msp.org/memocs/2017/5-1/p03.xhtml.

[85] M. Avellaneda, Optimal bounds and microgeometries for elastic two-phase composites, SIAM J. Appl. Math. 47 (1987) 1216–1228, https://doi.org/10.1137/0147082, https://epubs.siam.org/doi/10.1137/0147082, publisher: Society for Industrial and Applied Mathematics.